Renewable Energy 150 (2020) 578–588

Contents lists available at ScienceDirect

Renewable Energy

journal homepage: www.elsevier.com/locate/renene

Dynamic analysis of wave action on an OWC wave energy converter under the influence of viscosity

Rong-quan Wang [a, b], De-zhi Ning [a, b, *]

[a] State Key Laboratory of Coastal and Offshore Engineering, Dalian University of Technology, Dalian, 116024, China
[b] Offshore Renewable Energy Research Center, Dalian University of Technology, Dalian, 116024, China

ARTICLE INFO

Article history:
Received 29 May 2018
Received in revised form
31 December 2019
Accepted 2 January 2020
Available online 6 January 2020

Keywords:
OWC
Wave energy
Wave dynamics
Viscosity effect
HOBEM

ABSTRACT

Oscillating water column (OWC) device is one of the most promising wave energy converters (WECs). Besides the energy conversion efficiency, the survivability should also be considered for a design purpose in the process of wave energy exploitation. In the present study, by introducing the artificial viscous terms into the dynamic free surface boundary condition and Bernoulli equation, a fully nonlinear numerical model based on higher-order boundary element method (HOBEM) is adopted to model the wave dynamics of an OWC device. The viscosity effects on the wave force (i.e., ΔF) is investigated by comparing the predicted wave force by the numerical model with and without these viscous terms. The effects of the chamber geometry parameters, such as front wall draft, chamber width and opening ratio (i.e., air orifice width), on ΔF are investigated. The results indicate that the viscosity effect on the wave force on the seaside surface of the front wall is larger than that on its shoreside surface. The viscosity effect on the total horizontal wave force on the front wall increases with the increase of front wall draft in some extent. The influence of the viscosity on the horizontal wave force increases with opening ratio decreasing due to the increasing air pressure inside the chamber.

© 2020 The Authors. Published by Elsevier Ltd. This is an open access article under the CC BY-NC-ND license (http://creativecommons.org/licenses/by-nc-nd/4.0/).

1. Introduction

Marine renewable energy is considered to be a pollution-free power and can be a feasible alternative solution to the energy demands of isolated islands and remote communities [1]. Wave energy, one main type of marine renewable energy, is attractive especially in maritime countries due to its apparent superiorities with lots of wave energy converters (WECs) inventions [2]. Among those WECs, oscillating water column (OWC) systems stand out for two main reasons: technological simplicity and low maintenance costs [3,4]. First, the mechanism of OWC is simple: an OWC consists of a partially submerged chamber that subjects to wave action through an underwater opening and an air turbine. Wave action produces the oscillation of the water column inside the chamber, which forces the trapped air to enter and exit the chamber through the orifice to drive the turbine. The second good aspect is their lower maintenance costs when compared to other WECs, not only as a result of the aforementioned technological simplicity but also because there are no moving parts in direct contact with seawater.

In the recent decades, some excellent investigations have been performed on the hydrodynamic performance of various OWCs. Evans [5] developed a theoretical model to estimate the hydrodynamic efficiency of a fixed OWC device by assuming that the water column moves like a weightless piston. Thereafter, Evans [6] and Falnes and Mciver [7] improved the model by allowing the spatial variation of the internal free surface. Physical experiments were carried out to optimize the design parameters and improve the hydrodynamic performance of the OWCs, such as Morris-Thomas et al. [8], Dizadji and Sajadian [9], He et al. [10], Ning et al. [11] and Vyzikas et al. [12]. More recently, Ning et al. [13,14] reported that the hydrodynamic efficiency of the OWC device can be improved by introducing an dual-chamber structure based on a series of physical model tests. The experimental data were commonly used as validations of numerical or analytical models [15–20]. Compared to the experimental tests, numerical simulation is much more economical and faster. Thus, numerous nonlinear numerical models based on potential flow theory [21,22] and viscous flow theory [23–26] were developed to evaluate the hydrodynamic efficiency of the OWCs.

* Corresponding author. State Key Laboratory of Coastal and Offshore Engineering, Dalian University of Technology, Dalian, 116024, China.
E-mail addresses: rqwang@dlut.edu.cn (R.-q. Wang), dzning@dlut.edu.cn (D.-z. Ning).

https://doi.org/10.1016/j.renene.2020.01.007
0960-1481/© 2020 The Authors. Published by Elsevier Ltd. This is an open access article under the CC BY-NC-ND license (http://creativecommons.org/licenses/by-nc-nd/4.0/).

Besides the energy conversion efficiency, the survivability due to storm wave action is another important factor in the process of the WEC design and operation. Some OWC devices damaged by waves were ever reported, such as Osprey 1 wave power plant in Scotland [27] and Pico plant in Portugal [28,29]. However, there are less works on wave dynamics of OWC devices by comparison with those on hydrodynamic efficiency in the previous researches. Ashlin et al. [30] experimentally studied the horizontal and vertical wave forces on an OWC device, with special attention on the effects of the relative water depth and the wave steepness on the wave loads. Didier et al. [31] numerically investigated the total wave force and the wave force on the outside of the front wall of the OWC air chamber based on viscous flow theory and SPH method. The influence of the wave height on the wave forces was examined in their study. Ning et al. [32] numerically and experimentally investigated the effects of wave conditions and chamber geometry on the horizontal wave force on the front wall of an OWC device. To better understand the mechanisms lying beneath wave forces acting on the OWC device and provide a guidance for the device design and safe operation, further researches on the wave forces on OWC device are still needed. The CFD models based on the Navier-Stokes equations can consider the energy loss due to viscosity, however, both physical and numerical dissipations are mixed and difficult to separate in these models. The combination of the physical experiments and the improved potential flow model by introducing an adaptable artificial viscous term can well evaluate the viscosity influence on hydrodynamic efficiency [33]. Thus, as a continuous and extended work to the previous research [32], drawing on the similar method used to estimate the energy loss due to the wave nonlinearity and viscosity [33], the viscosity effect on the wave force is investigated by comparing the wave force estimated by the numerical model with and without the viscous terms in the dynamic free surface boundary condition and the Bernoulli equation in the present study. The effects of the chamber geometry such as front wall draft, chamber width and orifice width on the contribution of viscous terms to the wave loading are studied systematically over a wide range of wave conditions.

The rest of the present paper is organized as follows. The adopted numerical methodology is briefly introduced in Section 2. Then, the comparison between numerical results and experimental data, the role of chamber geometry in the viscosity effect on wave forces on the front wall are discussed in details in Section 3. Finally, the conclusions are summarized in Section 4.

2. Numerical methodology

Ning et al. [32] developed a potential numerical model to investigate wave dynamics of a land-fixed OWC wave energy converter. In the numerical model, an artificial viscous damping term $\mu_2\partial\phi/\partial n$ was applied to the dynamic free surface boundary condition inside the OWC chamber to model the effect of viscosity on the physical quantities inside the chamber (e.g., the free surface elevation and the dynamic pressure on the shoreside (internal) surface of the front wall) due to the flow separation and vortex shedding near the front wall which is proportional to the square of the flow velocity; and the artificial viscous term $\mu_2\partial\phi/\partial t$ was applied to the Bernoulli equation to consider the viscosity effect on the wave force on the shoreside surface of the front wall. The dynamic pressure along the surfaces of the front wall and the horizontal wave loads on the OWC device were considered. This potential numerical model is adopted in this study to predict the viscosity effect on wave dynamics of a land-fixed OWC wave energy converter, in which a linear pneumatic model was adopted to predict the air pressure imposed on the dynamic free surface inside the chamber; a boundary integral equation was founded based on the proposed boundary value problem; the mixed Eulerian-Lagrangian technique is used to describe the time-dependent free surface nodes and the HOBEM is adopted to solve the boundary integral equation; the acceleration potential method is applied to calculate the hydrodynamic pressure on the device. The underlying mathematical formulations and the numerical implementation are recommended to refer to Refs. [21,32] in detail.

Fig. 1 shows the simplified sketch of the problem in two-dimensions (2-D). The wave is generated by the inner sources at $x= 0$ and approaches towards a semi-submerged OWC device located at the right side of the numerical wave flume. A numerical beach is implemented at the left end of the numerical flume to minimize the reflected waves from the structure. The coordinate system used in this study is shown in Fig. 1. The x-axis is positive in the wave propagation direction with its origin at the inner source position, and the z-axis is positive upward with $z = 0$ at the mean free surface. B denotes the chamber width, C the front wall thickness, d the front wall draft, h the still water depth, h_c the chamber height, L_d the sponge layer length defined as 1.5 times the incident wavelength (i.e., 1.5L, where L is the wavelength) and L_o the orifice width. The computational domain Ω boundary includes free surface Γ_{fo} outside the chamber and Γ_{fi} inside the chamber and solid boundaries (i.e. bottom boundary Γ_d and body boundary Γ_b). S_{o1}~ S_{o3} and S_{i1}~ S_{i3} are pressure measurement points distributed on seaside (external) and shoreside (internal) surfaces of the front wall. G_1 and G_2 are the surface elevation measurement points along the outer and inner surface (i.e., the seaside and shoreside surface) of the front wall. The free surface elevations at G_3 and G_4 are used to calculate the reflection coefficient, and the distance between the two points is 1.5 m with G_3 1.0 m away from the outside edge of the front wall.

Once the velocity potential ϕ on the OWC device is obtained, the corresponding pressure can be calculated from the Bernoulli equation. In the present study, only the horizontal wave force on the front wall is considered due to the fact that the front wall thickness is much smaller than its draft. Therefore, the two horizontal wave force components exerted on the two surfaces of the front wall, F_i and F_o, can be obtained from the following integration of the pressure over the wetted surface of the wall, Γ_b, as follows:

$$F_i = \int_{\Gamma_b} p_w n_x d\Gamma = -\rho \int_{\Gamma_b} \left(\frac{\partial \phi}{\partial t} + g\eta + \frac{1}{2}|\nabla\phi|^2 + \frac{p_a}{\rho} \right) n_x d\Gamma \text{ , shoreside component} \quad (1)$$

$$F_o = \int_{\Gamma_b} p_w n_x d\Gamma = -\rho \int_{\Gamma_b} \left(\frac{\partial \phi}{\partial t} + g\eta + \frac{1}{2}|\nabla\phi|^2 - \mu_2 \frac{\partial \phi}{\partial t} \right) n_x d\Gamma \text{ , seaside component} \quad (2)$$

where p_w represents the hydrodynamic pressure, ϕ the velocity potential, η the free surface elevation, ρ the water density, n_x the normal vector in the x direction and t the time, the damping coefficient μ_2 is determined by trial and error method by comparison with the measured data. Eq. (1) is used to calculate the wave force on the shoreside surface of the front wall, in which the pressure term (i.e., p_a/ρ) on the right side represents the air pressure inside the chamber. Eq. (2) is used to estimate the wave force on the seaside surface of the front wall, in which the artificial viscous term (i.e., $\mu_2\partial\phi/\partial t$) is introduced to consider the viscosity effect.

The total horizontal wave force F_h on the front wall is the sum of F_o and F_i:

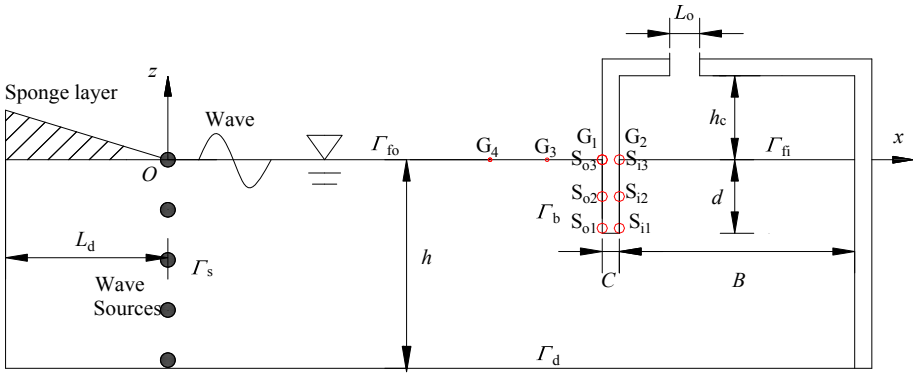

Fig. 1. Sketch of the numerical wave flume.

$$F_h = F_o + F_i \tag{3}$$

To consider the viscosity effect on the wave force, following the method used in estimating the energy loss due to wave nonlinearity and viscosity [33], the normalized difference between the wave force estimated by the numerical model without the viscous term (i.e., $\mu_2 = 0$ in both dynamic boundary condition expression and Bernoulli equation) and with the viscous term is given by

$$\Delta F = \frac{|F_{NV} - F_V|}{\rho g d A_i} \tag{4}$$

where F_{NV} denotes the wave force estimated by the present model without the viscous term (i.e., $\mu_2 = 0$) and F_V denotes the predicted wave force with the viscous term, A_i is the incident wave amplitude.

3. Results and discussion

In the present study, the experiments performed by Ning et al. [32] is still considered and all the simulations are performed with a constant water depth of $h = 0.8$ m and a constant incident wave amplitude of $A_i = 0.03$ m. Generally, OWC devices are designed with a chamber width 1/10 of the wavelength to ensure its good hydrodynamic performance. However, the OWC device experiences various wave conditions in the real sea states. Thus, the incident wave periods T in the range of 1.037 s ~ 2.350 s with its corresponding wavelength change from 1.67 m to 5.94 m are chosen in the present study. The relative chamber widths B/L in the range of 0.09 ~ 0.51 are investigated.

3.1. Comparison of numerical and experimental results

In the present subsection, the geometrical parameters: chamber width $B = 0.55$ m, front wall draft $d = 0.14$ m, orifice width $L_o = 0.0036$ m (with the same area of the circular-shaped orifice diameter $D = 0.06$ m in the experiment in 3-D), are chosen. The same geometrical parameter and wave conditions were used in the previous studies [11,21,33], the numerical model with a proper linear pneumatic damping coefficient (i.e., $C_{dm} = 9.5$) and viscous damping coefficient (i.e., $\mu_2 = 0.2$) can capture the hydrodynamics at a fixed OWC device [11], such as surface elevation, air pressure inside the chamber and hydrodynamic efficiency well. The numerical model can also capture the observed dynamic pressure on the front wall well by introducing an artificial viscous term in the equation for calculating the dynamic pressure [32]. In the present study, to check the accuracy of the simulated wave forces with the viscous terms considered, the comparisons between the predicted and measured dynamic pressures at different locations on the front wall are carried out.

Fig. 2 shows the comparison of the time series of the predicted and measured dynamic pressures with wave period $T = 1.183$ s and 1.838 s. Overall, the dynamic pressures on the front wall are well resolved by the numerical model, apart from some minor discrepancies at the maximum and minimum pressures (i.e., at S_{o1} for wave period $T = 1.183$ s) that might be caused by the vortex shedding near the front wall edge [34]. Fig. 3(a) and (b) show the time series of the surface elevations along the seaside (i.e., at G_1) and shoreside (i.e., at G_2) surfaces of the front wall for wave periods of $T = 1.183$ s and 1.838 s, respectively. Under the action of short waves (i.e., $T = 1.183$ s), as shown in Fig. 3(a), the maximum surface elevation at G_1 is larger than that at G_2, which directly lead to a larger dynamic pressure on the seaside surface of the front wall as shown in Fig. 2(a) and (b). While under the action of the long waves (i.e., $T = 1.838$ s), the surface elevations along both surfaces of the front wall are almost in phase with each other and have similar amplitudes as can be seen from Fig. 3(b). As a consequence, the dynamic pressures at the same vertical position on the two sides of the front wall (e.g., S_{o1} and S_{i1}) are similar with each other as shown in Fig. 2(c) and (d). Additionally, the nonlinearity and asymmetry of the dynamic pressure curves which resulting from the wave-structure interaction and the enhanced wave nonlinearity are observed from Fig. 2. Therefore, further comparisons of the absolute maximum and minimum values of the predicted dynamic pressures and the experiments are performed.

Fig. 4 shows the absolute values of the averaged maximum and minimum dynamic pressures at different locations on the front wall of the chamber versus dimensionless wave number kh. The signals within 5 wave periods interval ($t = 10T$ ~ $15T$) are used for averaging. It is evident from these figures that overall good agreements are achieved between the model results and laboratory measurements. The measuring point S_{o3} is at still water surface. The pressures at S_{o3} are zero when the free surface is below the still water surface, thus the minimum value of dynamic pressure at S_{o3} is not shown. A significant effect of the wave frequency on the dynamic pressure can be observed. Both simulations and the experiments show that the maximum and minimum values of the pressure on the seaside surface of the front wall (i.e., S_{o1}, S_{o2} and S_{o3}) firstly decrease with increasing kh in a certain kh range and then increase with further increasing kh. This is mainly due to the fact that the wave pressure on the seaside surface of the front wall directly depends on the wave outside the chamber (i.e., the reflection wave). As shown in Fig. 5, the reflection coefficient K_r ($K_r = A_r/A_i$, where A_r is the amplitude of the reflected wave) also

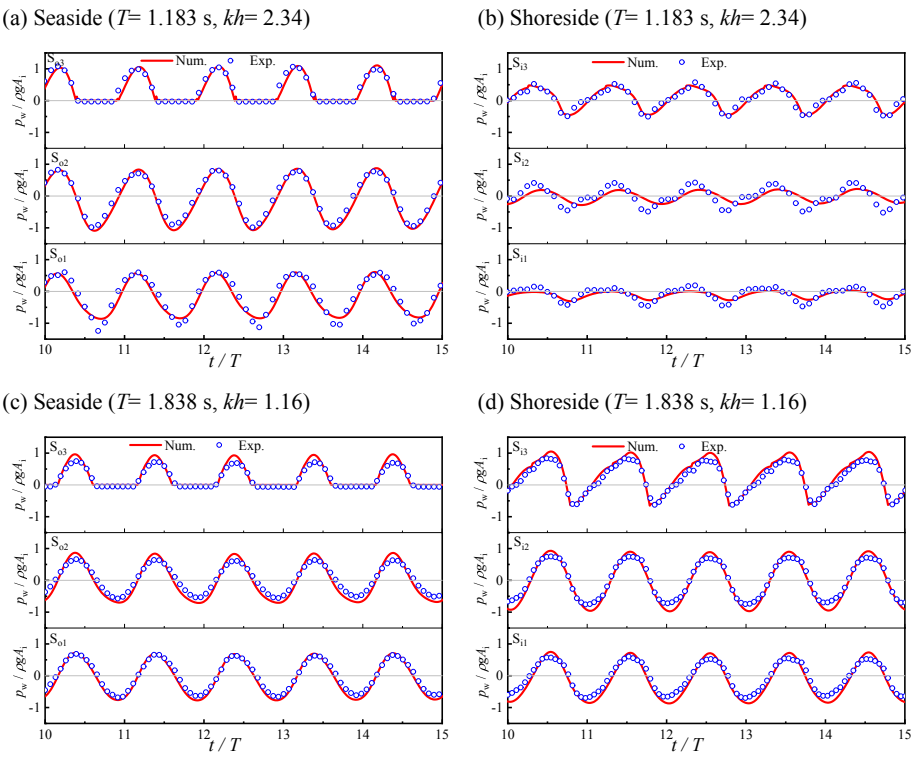

Fig. 2. Comparisons of the predicted and measured normalized dynamic pressures at different measuring locations of seaside (a, c) and shoreside (b, d) surface of the front wall: (a) & (b) for $T = 1.183$ s; (c) & (d) for $T = 1.838$ s (chamber width $B = 0.55$ m, front wall draft $d = 0.14$ m, orifice width $L_o = 0.0036$ m (circular-shaped orifice diameter $D = 0.06$ m in the experiment)).

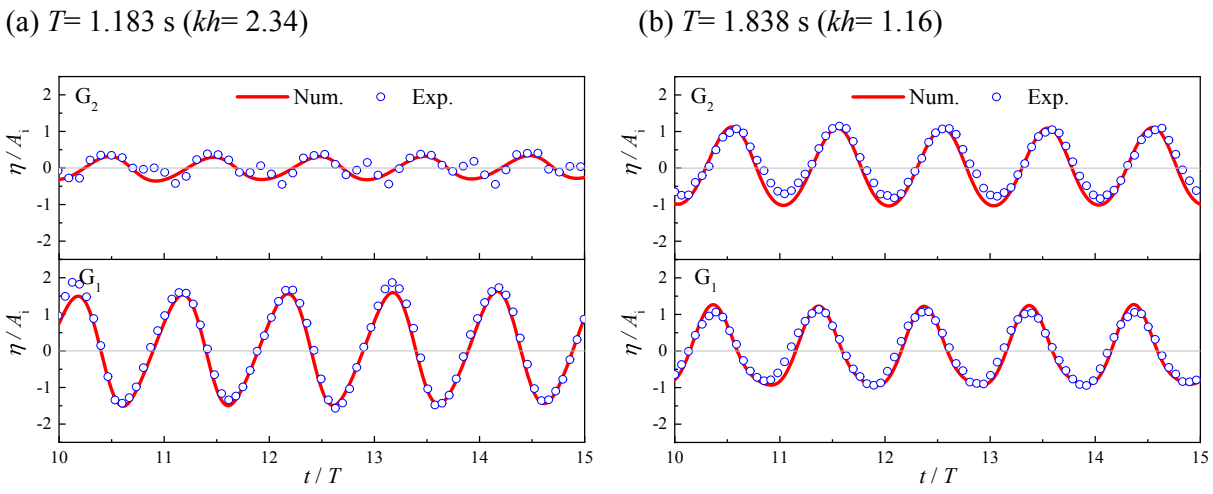

Fig. 3. Time series of the surface elevation at G_1 and G_2 for different wave periods $T = 1.183$ s and 1.838 s (chamber width $B = 0.55$ m, front wall draft $d = 0.14$ m, orifice width $L_o = 0.0036$ m (circular-shaped orifice diameter $D = 0.06$ m in the experiment)).

decreases with increasing *kh* to its minimum and then increases with further increasing *kh*. The absolute values of the maximum and minimum pressures on the shoreside surface of the front wall (i.e., S_{i1}, S_{i2} and S_{i3}) decreases with increasing *kh* continuously. It should be noted that, due to the nonlinearity and asymmetry, the absolute maximum and minimum values of the pressure time series differ from each other, especially for the dynamic pressure on the seaside surface of the front wall. The minimum value is larger than the maximum value for some wave conditions. For example, at point S_{o1}, the minimum pressure is larger than the maximum pressure when $kh > 1.4$ as shown in Fig. 4(e).

3.2. Viscosity effects on wave force

In this subsection, the effects of viscosity on horizontal wave force are investigated. Fig. 6 shows the comparison of the wave forces predicted by the numerical model with and without the viscous term, i.e., $F_{(V)}$ and $F_{(NV)}$. In the figures, F_{hc} and F_{ht} represent the absolute averaged values of the total horizontal wave force crests (maximum) and troughs (minimum), respectively; F_{oc} and F_{ot} represent the absolute averaged values of the crests and troughs of the seaside component of the horizontal wave force on the of the front wall, respectively; and F_{ic} and F_{it} represent the absolute

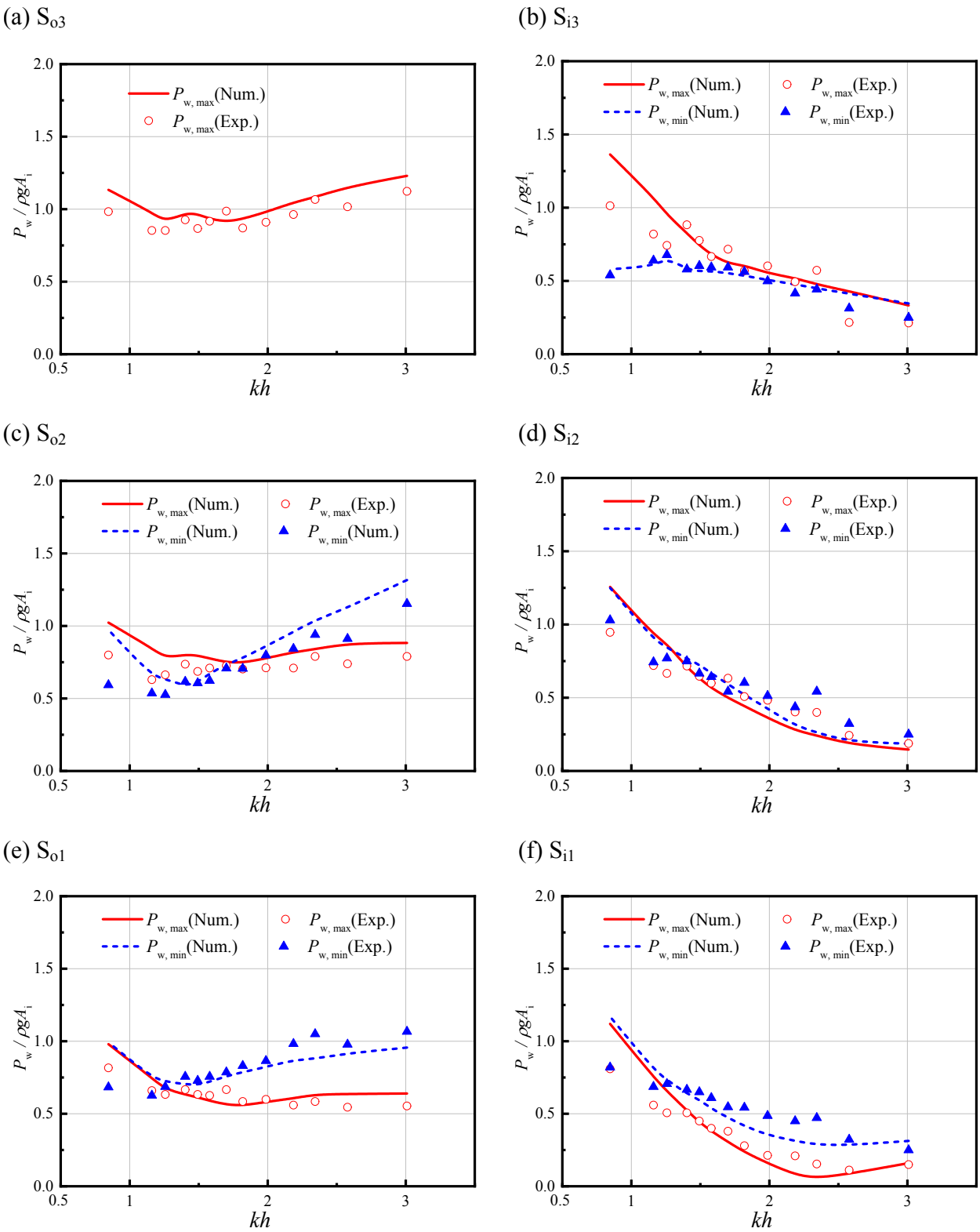

Fig. 4. Normalized absolute values of the maximum and minimum dynamic pressures at different locations on the front wall (S_{o1}~ S_{o3} on the seaside and S_{i1}~ S_{i3} on the shoreside surface) versus dimensionless wave number kh for chamber width B= 0.55 m, front wall draft d = 0.14 m and orifice width L_o = 0.0036 m (circular-shaped orifice diameter D = 0.06 m in the experiment).

averaged values of the crests and troughs of the shoreside component of the horizontal wave force on the front wall, respectively. It can be seen that F_{oc} and F_{ot} initially decrease to its minimum and then increase with increasing kh, while F_{ic} and F_{it} decrease with the increase of kh due to the wave transmission ability decreasing. For the total wave force F_h, F_{hc} increases with the

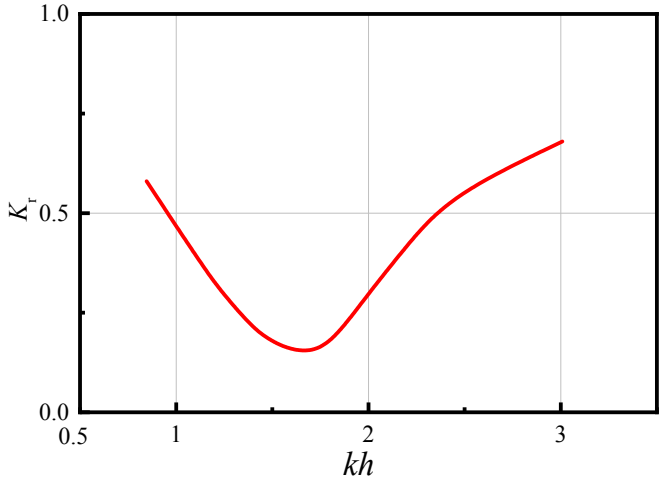

Fig. 5. Reflection coefficient K_r versus kh for chamber width B= 0.55 m, front wall draft d = 0.14 m and orifice width L_o = 0.0036 m.

increase of kh, and F_{ht} increases firstly to its maximum and then decreases with kh due to the phase difference between F_i and F_o. The total wave force F_h and the wave force on the seaside surface of the front wall F_o without viscous term (i.e., F_{NV}) are usually larger than that with the viscous term (i.e., F_V). The viscosity, however, has little effect on the wave force on the shoreside surface of the front wall F_i. It should be noted that, though the minimum value of the dynamic pressure is larger than its maximum value for some cases as described before, the maximum value of the wave force is larger than its minimum value for the most cases as shown in Fig. 6(a) and (b). Thus, in the rest of the paper, the maximum values of the wave forces are mainly considered.

3.3. Effects of geometrical parameters

In this subsection, the influence of the geometry parameters, i.e., the front wall draft d, the chamber width B and the air orifice width L_o, on the horizontal wave forces on the front wall of the OWC device are investigated individually. To quantify the viscosity effects on the wave force, the relative difference between the predicted wave force by the numerical model without and with the viscous term (i.e., $\Delta F = |F_{NV} - F_V|/\rho g d A_i$) is examined.

3.3.1. Front wall draft

The influence of the front wall draft on ΔF (i.e., the relative difference between the wave force estimated by the numerical model with and without the viscous term) is analyzed by varying the front wall draft (d = 0.14, 0.17 and 0.25 m, i.e., the relative submerged front wall depth d/h = 0.175, 0.213 and 0.25) and keeping the other geometry parameters constant as B = 0.55 m and L_o = 0.0036 m.

Fig. 7 shows the effects of the front wall draft on ΔF for three simulated front wall drafts. Generally, ΔF_{oc} decreases first to its minimum and then increases with kh increasing as shown in Fig. 7(a). Note that, the local maximums are observed in the resonant frequency region, which is near to kh = 1.5 according to the previous experimental study [11]. In the high-frequency region, the viscosity effect on the shoreside component of the wave force on the front wall increases with the front wall draft increasing due to the increasing viscous wet surface. As shown in Fig. 7(b), ΔF_{ic} is much smaller than ΔF_{oc}, i.e., the influence of the viscosity on the shoreside component of the wave force on the front wall is weaker than that on its seaside component. For small scale structure ($C/L < 0.2$), viscosity effects on the hydrodynamics are prominent, and more apparent on the seaside surface than on the shoreside surface, which can also be observed from CFD simulations [24,35]. The local maximums are also observed in the resonant frequency region in Fig. 7(b). In addition, the change of the front wall draft has little effect on ΔF_{ic}.

According to the previous velocity field studies on the OWC device [36–38], vortex shedding occurs at the lower lip of the OWC front wall. The flow velocity under the front wall opening is not uniform distribution and only part of it is active [35]. Due to the piston motion of the water column inside the chamber, the flow velocity direction around the front wall is a U-shape, i.e., the flow velocity direction around the front wall is tangent to the front wall surface. The viscosity effect is proportional to the square of flow velocity [39] and the flow velocity U is proportional to A_i/T [40]. Therefore, the viscosity effects can be described by the surface-elevation variation rate $\eta' = (\eta_{max} + |\eta_{min}|)/2T$, where η_{max} and η_{min} represent the maximum and the minimum of the free surface elevation, respectively. Fig. 8(a) and (b) show the surface-elevation variation rate at G_1 and G_2, respectively. It can be seen that the free-surface variation rate at G_1 increases with the front wall draft and the free-surface variation rate at G_2 is not sensitive to the change of the front draft in the range of the present study. This is further evidence that the viscosity effect on F_{oc} increases with the front wall draft increasing, while it has little influence on F_{ic}.

Generally, ΔF_{hc} increases with increasing kh as shown in Fig. 7(c). Due to the phase shift between F_o and F_i as shown in Fig. 9, $F_h = F_o + F_i$ shows different trend from F_o and F_i. Thus, unlike ΔF_{oc} and ΔF_{ic}, ΔF_{hc} displays a declining trend after its slight increase in the resonant frequency region. In addition, ΔF_{hc} increases with

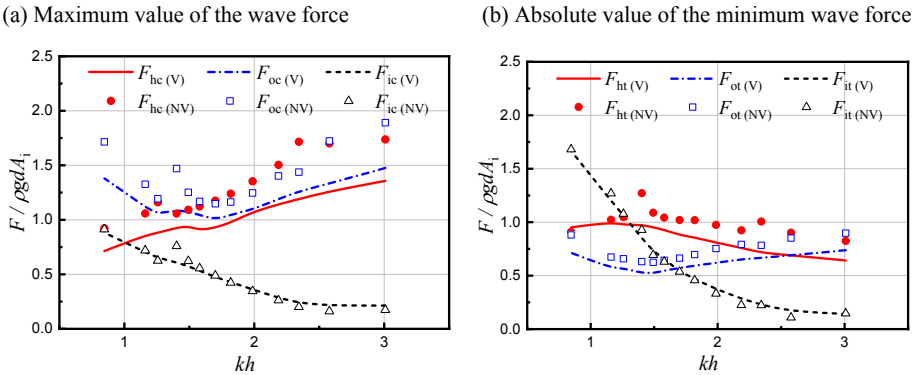

Fig. 6. Viscosity effect on the total horizontal wave force on the front wall and its two components for dimensionless wave number kh for chamber width B= 0.55 m, front wall draft d = 0.14 m and orifice width L_o = 0.0036 m.

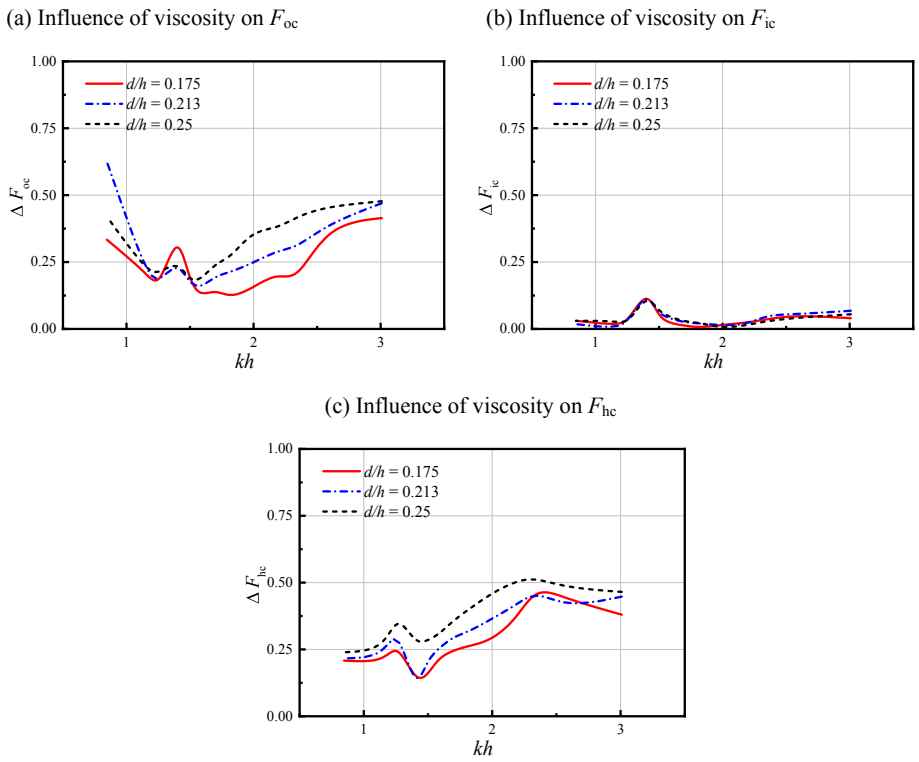

Fig. 7. Effects of viscosity on (a) seaside and (b) shoreside force components, and (c) the total wave force on the front wall versus dimensionless wave number *kh* for relative submerged front wall depth d/h = 0.175, 0.213 and 0.25.

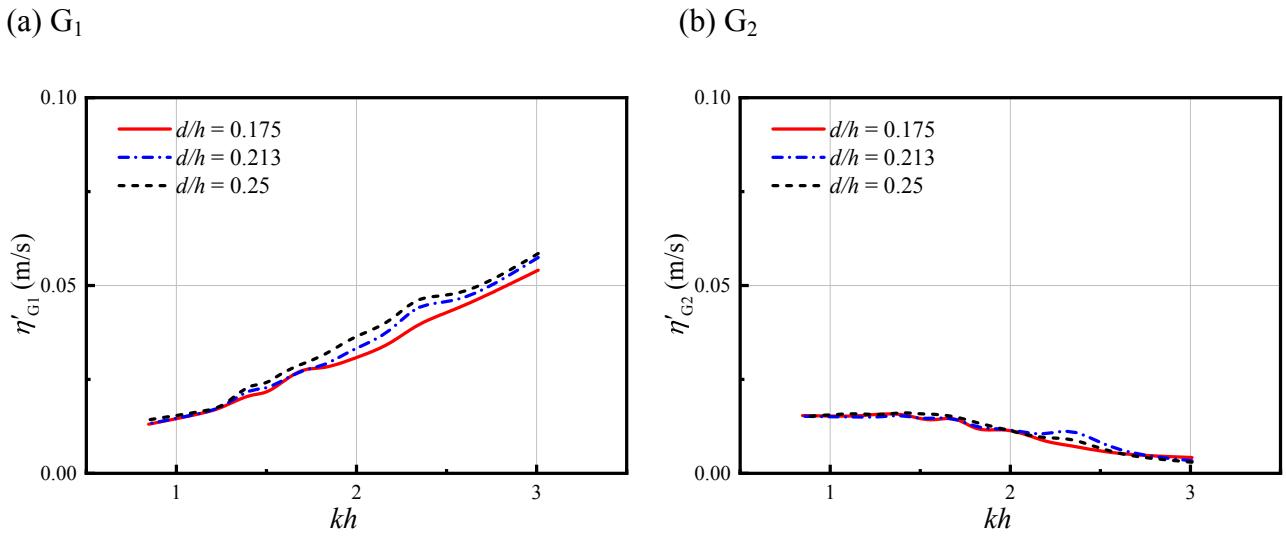

Fig. 8. Variation of the measured free surface elevation rate at (a) G_1 and (b) G_2 for relative submerged front wall depth d/h = 0.175, 0.213 and 0.25.

increasing front wall draft as illustrated in Fig. 7(c). That is, the viscosity effect on the maximum of the total wave force increases with the front wall draft increasing. According to López et al. [38], the turbulent kinetic energy increases with the increase of tidal level. In the present considered scope, the increase of the front wall draft is equivalent to an increase of tidal level in some extent. The flow velocity increases with the increase of the front wall draft as could also be seen in Fig. 8(a), which leads to an increase of flow separation and vortex shedding. As a consequence, the viscosity effects on the wave force increase with front wall draft.

3.3.2. Chamber width

By keeping the front wall draft d = 0.14 m and orifice width L_o= 0.0036 m constants, the effect of chamber width on ΔF is investigated. Three different chamber widths B = 0.55, 0.70 and 0.85 m are considered, i.e., the corresponding relative chamber widths B/L under different wave periods (i.e., different wavelengths) are in the range of (0.09 ~ 0.33), (0.12 ~ 0.42) and (0.14 ~ 0.51), respectively.

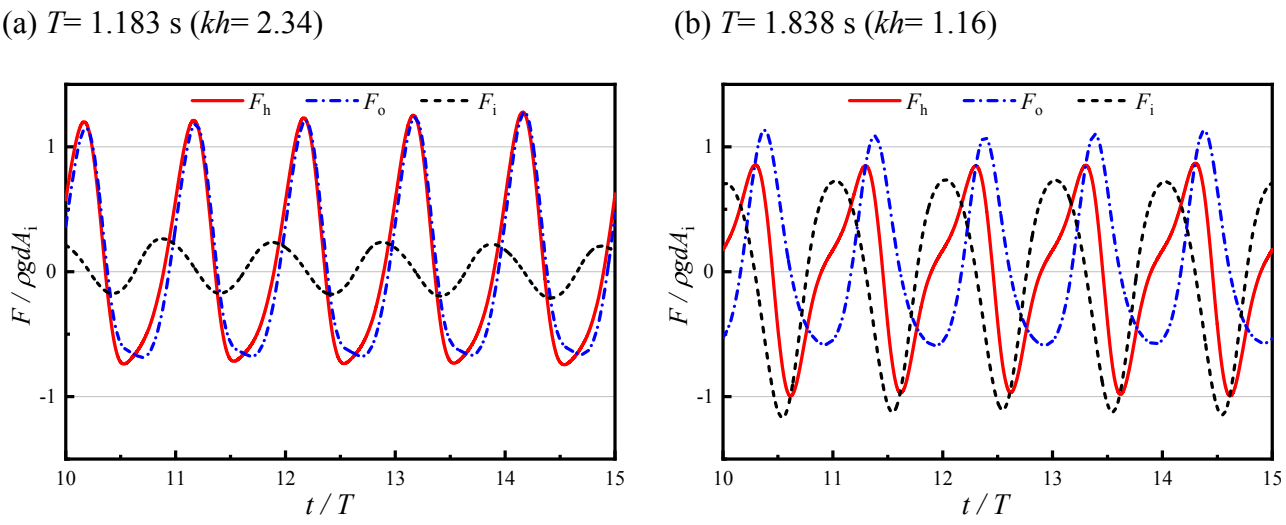

Fig. 9. Time series of the horizontal wave force on the front wall for different wave periods T = 1.183 s and 1.838 s (chamber width B= 0.55 m, front wall draft d = 0.14 m and orifice width L_o = 0.0036 m).

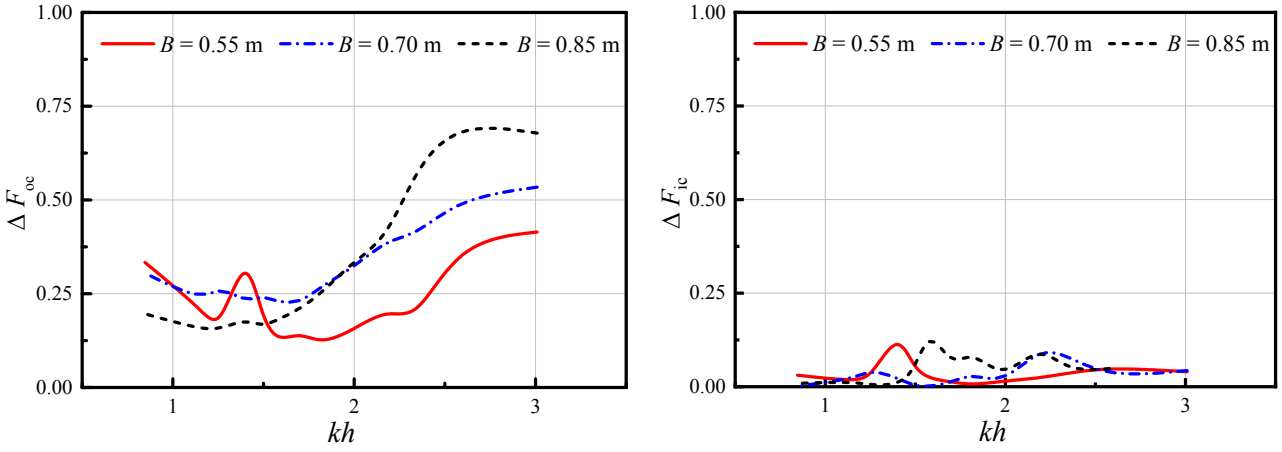

(c) Influence of viscosity on F_{hc}

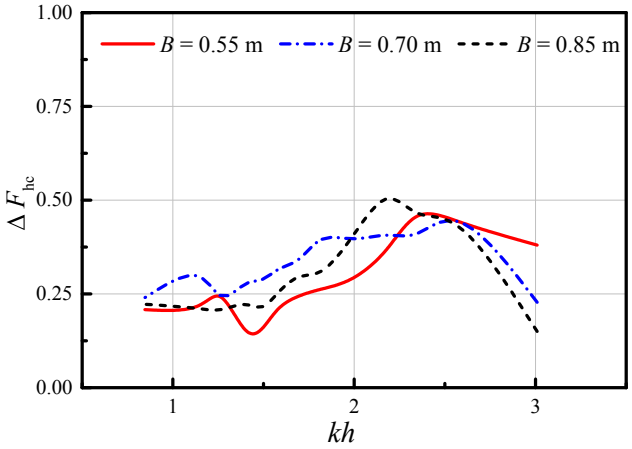

Fig. 10. Effects of viscosity on (a) seaside and (b) shoreside force components, and (c) the total wave force on the front wall versus dimensionless wave number kh for the chamber widths B = 0.55, 0.70 and 0.85 m.

Fig. 10(a), (b) and (c) show the effects of the chamber width on ΔF_{oc}, ΔF_{ic} and ΔF_{hc}, respectively. As it can be seen from Fig. 10(a), the effect of the viscosity on the ΔF_{oc} is relatively small in the low-frequency region. While in the high-frequency region, the influence of the viscosity on F_{oc} is large, and it increases with the chamber width increasing. However, the influence of the chamber width on the wave force on the shoreside surface of the front wall (i.e., F_{ic}) is very limited as illustrated in Fig. 10(b). For the influence of the viscosity on the total wave force F_{hc}, it is found that ΔF_{hc} decreases with kh when kh is larger than a certain value as shown in Fig. 10(c). According to the previous experimental study [11], the seiching phenomenon is excited when the relative chamber width B/L is 0.5 and the free-surface motion inside the chamber is a typically standing wave characteristics with the front wall at its antinode. The total volume of the water column inside the chamber is nearly not changed under this situation. Thus, there is nearly no water exchange between the OWC chamber and the sea. That is, there is nearly no flow produced through the front wall lower lip. As a consequence, the viscosity effects due to the flow separation reach the minimum. Thus, the influence of the viscosity on the total horizontal wave force on the front wall becomes weaker as the relative chamber width B/L is closer to 0.5. For example, the effect of viscosity on the total wave force, i.e., ΔF_{hc}, is the smallest in the case of $B = 0.85$ m and $kh = 3.01$ (i.e., $B/L = 0.51$) in Fig. 10(c).

3.3.3. Air orifice size

An air orifice is introduced to represent the power take-off system of the OWC device in the present study. According to the previous experimental study by Ning et al. [11], the effect of the orifice size on the hydrodynamic efficiency is significant due to the fact that it influences the free surface elevation and air pressure in the air chamber greatly. The size of an air orifice is often described by the opening ratio $\varepsilon = S_o/S$, where S_o and S represent the cross-section areas of the orifice and the still water free surface inside the chamber, respectively. In the present study, the effects of the orifice scale on ΔF are investigated and shown in Fig. 11 by keeping the chamber width $B = 0.55$ m and front wall draft $d = 0.14$ m constants. Three opening ratios $\varepsilon = 0.29\%$, 0.66% and 1.17% corresponding to the orifice width of $L_o = 0.0016$, 0.0036 and 0.0064 m are considered.

The influence of the opening ratio on the ΔF_{oc} increases with the decrease of the opening ratio as shown in Fig. 11(a). As described before, the viscosity effect is proportional to the flow velocity below the front wall lower lip, and the flow velocity further responses to the motion of the free surface near the front wall. The surface-elevation variation rate at G_1 increases with the decrease of the opening ratio as shown in Fig. 12(a). As a consequence, the viscosity effect on the wave force on the seaside surface of the front wall, i.e., F_{oc}, becomes stronger with the opening ratio decreasing. The viscosity effect on F_{ic} and the effect of the opening ratio on ΔF_{ic} are very limited as shown in Fig. 11(b). However, in the resonant frequency region, the viscosity effect on F_{ic} increases with the opening ratio increasing. This is because the motion of surface elevation inside the chamber become stronger with the increase of opening ratio as shown in Fig. 12(b). Additionally, the smaller opening ratio leads to a larger air pressure inside the air chamber [32], which is equivalent to adding a larger motion damping to the water column. This can further lead to a smaller flow velocity inside the chamber, i.e., a weaker motion of the free surface inside the chamber. Thus, the dynamic wave force exerted on the front wall is mainly owing to the wave force on the seaside surface of the front wall as also can be seen in Fig. 13, which shows the total wave force F_h and its components F_{oc} and F_{ic} versus kh for open ratio $\varepsilon = 0.29\%$. Combining with the former analysis, the viscosity effect on the wave force on the seaside surface of the front wall increases with the decrease of opening ratio. As a consequence, the influence of

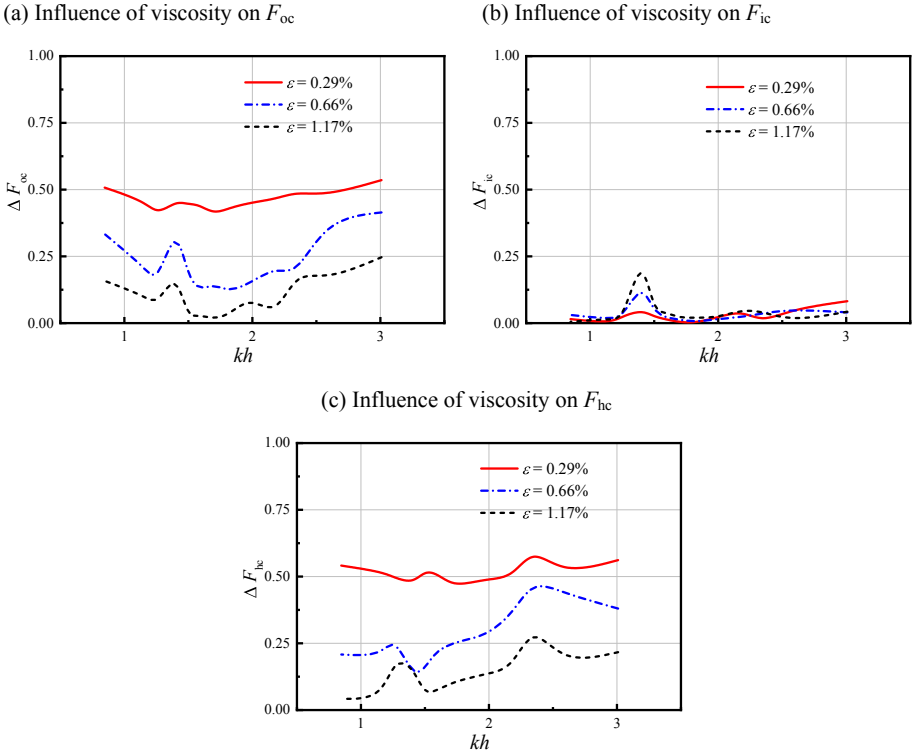

Fig. 11. Effects of viscosity on (a) seaside and (b) shoreside force components, and (c) the total wave force on the front wall versus dimensionless wave number kh for the open ratios ε= 0.29%, 0.66% and 1.17%.

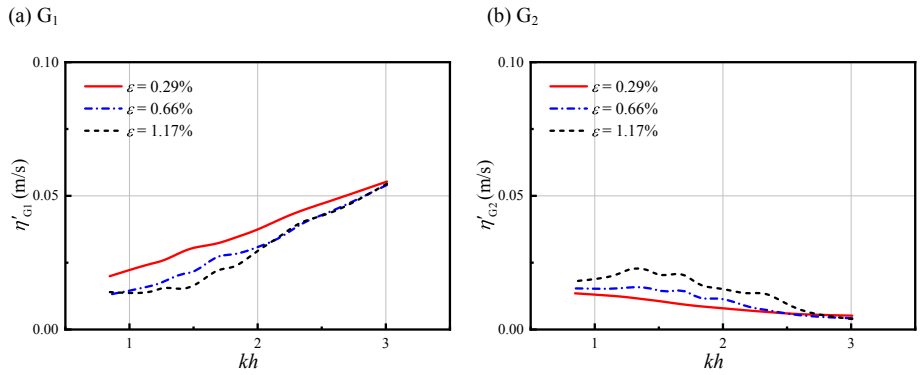

Fig. 12. Variation of the measured free surface elevation rate at (a) G_1 and (b) G_2 for the open ratios ε= 0.29%, 0.66% and 1.17%.

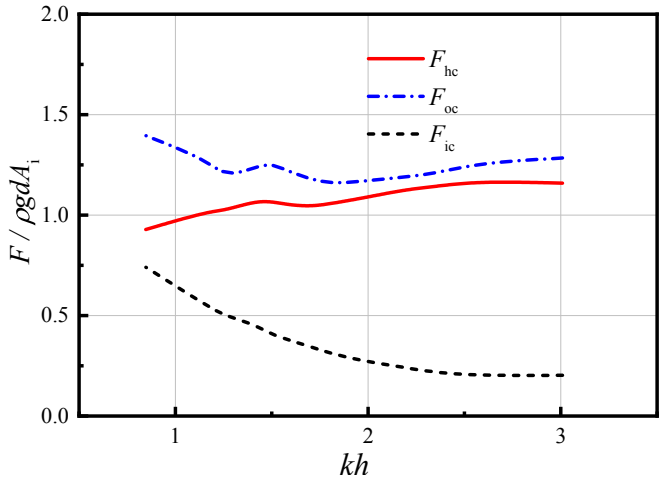

Fig. 13. The total wave force F_{hc} and its components F_{oc} and F_{ic} versus kh for chamber width B= 0.55 m, front wall draft d = 0.14 m and open ratio ε= 0.29%.

the viscosity on F_{hc} increases with the opening ratio decreasing as shown in Fig. 11(c).

4. Conclusions

A fully-nonlinear numerical wave flume based on the potential-flow theory and the time-domain higher-order boundary element method (HOBEM) is applied to investigate the wave force on the front wall of a land-fixed OWC device with special attention on the influence of viscosity. The viscosity effect on the wave force (i.e., ΔF) is investigated by comparing the predicted wave force without and with the artificial viscous term. The effects of the chamber geometry parameters (i.e., front wall draft, chamber width and opening ratio) on ΔF are investigated. The following conclusions can be obtained.

The viscosity effect on the wave force exerted on the seaside surface of the front wall is relatively larger than that on the shoreside surface of the front wall. The viscosity effect on the total horizontal wave force increases with the increase of front wall draft due to the increasing flow separation and vortex shedding in the present considered scope. The influence of the viscosity on the total horizontal wave force on the front wall becomes weaker when kh is larger than a certain value (i.e., the relative chamber width B/L approaching 0.5 in the present study). Due to the fact that the larger air pressure adds damping to the water column, the smaller opening ratio leads to a larger influence of the viscosity on total horizontal wave force on the front wall of the OWC device.

The results of the present study allow one to better understand the controlling factors of the wave forces on the OWC device and provide guidance for the device design and safe operation. And the comparison analysis method can be extended to other kinds of wave energy devices and maritime structures.

Declaration of competing interest

The authors declare that they have no known competing financial interests or personal relationships that could have appeared to influence the work reported in this paper.

CRediT authorship contribution statement

Rong-quan Wang: Conceptualization, Methodology, Validation, Investigation, Writing - original draft. **De-zhi Ning:** Conceptualization, Resources, Supervision, Writing - review & editing.

Acknowledgment

This work was supported by the National Natural Science Foundation of China (Grant Nos. 51679036 and 51761135011) and the Project Funded by China Postdoctoral Science Foundation (Grant No. 2019TQ0048).

References

[1] A. Clement, P. McCullen, A. Falcao, A. Fiorentino, F. Gardner, K. Hammarlund, G. Lemonis, T. Lewis, K. Nielsen, S. Petroncini, M.T. Pontes, P. Schild, B.O. Sjostrom, H.C. Sorensen, T. Thorpe, Wave energy in Europe: current status and perspectives, Renew. Sustain. Energy Rev. 6 (5) (2002) 405–431.
[2] A.F.O. Falcão, Wave energy utilization: a review of the technologies, Renew. Sustain. Energy Rev. 14 (3) (2010) 899–918.
[3] Y.M.C. Delauré, A. Lewis, 3D hydrodynamic modelling of fixed oscillating water column wave power plant by a boundary element methods, Ocean Eng. 30 (3) (2003) 309–330.
[4] T.V. Heath, A review of oscillating water columns, Phil. Trans. R. Soc. A: Math. Phys. Eng. Sci. 370 (1959) (2012) 235–245.
[5] D.V. Evans, The oscillating water column wave-energy device, IMA J. Appl. Math. 22 (4) (1978) 423–433.
[6] D.V. Evans, Wave-power absorption by systems of oscillating surface pressure distributions, J. Fluid Mech. 114 (1982) 481–499.
[7] J. Falnes, P. Mciver, Surface-wave interactions with systems of oscillating bodies and pressure distributions, Appl. Ocean Res. 7 (4) (1985) 225–234.
[8] M.T. Morris-Thomas, R.J. Irvin, K.P. Thiagarajan, An investigation into the hydrodynamic efficiency of an oscillating water column, J. Offshore Mech. Arct. Eng. - Trans. ASME 129 (4) (2007) 273–278.
[9] N. Dizadji, S.E. Sajadian, Modeling and optimization of the chamber of OWC system, Energy 36 (5) (2011) 2360–2366.
[10] F. He, Z.H. Huang, A.W.K. Law, An experimental study of a floating breakwater with asymmetric pneumatic chambers for wave energy extraction, Appl. Energy 106 (2013) 222–231.
[11] D.Z. Ning, R.Q. Wang, Q.P. Zou, B. Teng, An experimental investigation of

hydrodynamics of a fixed OWC Wave Energy Converter, Appl. Energy 168 (2016) 636–648.
[12] T. Vyzikas, S. Deshoulieres, M. Barton, O. Giroux, D. Greaves, D. Simmonds, Experimental investigation of different geometries of fixed oscillating water column devices, Renew. Energy 104 (2017) 248–258.
[13] D.-z. Ning, R.-q. Wang, L.-f. Chen, K. Sun, Experimental investigation of a land-based dual-chamber OWC wave energy converter, Renew. Sustain. Energy Rev. 105 (2019) 48–60.
[14] D.-z. Ning, Y. Zhou, R. Mayon, L. Johanning, Experimental investigation on the hydrodynamic performance of a cylindrical dual-chamber Oscillating Water Column device, Appl. Energy 260 (2020).
[15] D.J. Wang, M. Katory, Y.S. Li, Analytical and experimental investigation on the hydrodynamic performance of onshore wave-power devices, Ocean Eng. 29 (8) (2002) 871–885.
[16] C.H. Xu, Z.H. Huang, Z.Z. Deng, Experimental and theoretical study of a cylindrical oscillating water column device with a quadratic power take-off model, Appl. Ocean Res. 57 (2016) 19–29.
[17] F. Mahnamfar, A. Altunkaynak, Comparison of numerical and experimental analyses for optimizing the geometry of OWC systems, Ocean Eng. 130 (2017) 10–24.
[18] A. Elhanafi, G. Macfarlane, A. Fleming, Z. Leong, Experimental and numerical investigations on the hydrodynamic performance of a floating–moored oscillating water column wave energy converter, Appl. Energy 205 (2017) 369–390.
[19] A. Elhanafi, G. Macfarlane, A. Fleming, Z. Leong, Experimental and numerical measurements of wave forces on a 3D offshore stationary OWC wave energy converter, Ocean Eng. 144 (2017) 98–117.
[20] K. Rezanejad, C. Guedes Soares, I. López, R. Carballo, Experimental and numerical investigation of the hydrodynamic performance of an oscillating water column wave energy converter, Renew. Energy 106 (2017) 1–16.
[21] D.Z. Ning, J. Shi, Q.P. Zou, B. Teng, Investigation of hydrodynamic performance of an OWC (oscillating water column) wave energy device using a fully nonlinear HOBEM (higher-order boundary element method), Energy 83 (2015) 177–188.
[22] G.D. Gkikas, G.A. Athanassoulis, Development of a novel nonlinear system identification scheme for the pressure fluctuation inside an oscillating water column-wave energy converter Part I: theoretical background and harmonic excitation case, Ocean Eng. 80 (2014) 84–99.
[23] A. Kamath, H. Bihs, O.A. Arntsen, Numerical investigations of the hydrodynamics of an oscillating water column device, Ocean Eng. 102 (2015) 40–50.
[24] Y.L. Zhang, Q.P. Zou, D. Greaves, Air–water two-phase flow modelling of hydrodynamic performance of an oscillating water column device, Renew. Energy 41 (2012) 159–170.
[25] P.R.F. Teixeira, D.P. Davyt, E. Didier, R. Ramalhais, Numerical simulation of an oscillating water column device using a code based on Navier–Stokes equations, Energy 61 (2013) 513–530.
[26] Y.Y. Luo, J.R. Nader, P. Cooper, S.P. Zhu, Nonlinear 2D analysis of the efficiency of fixed Oscillating Water Column wave energy converters, Renew. Energy 64 (2014) 255–265.
[27] HeraldScotland, Storm wrecks wave-power Osprey. http://www.heraldscotland.com/news/12089535.Storm_wrecks_wave_power_Osprey/, 1995.
[28] K. Monk, Forecasting for Control and Environmental Impacts of Wave Energy Converters, School of Marine Science and Engineering, Plymouth University, 2015.
[29] A.F.O. Falcão, L.M.C. Gato, A.J.N.A. Sarmento, A. Brito-Melo, The Pico OWC wave power plant: its life from conception to closure 1986–2018, in: Advances in Renewable Energies Offshore: Proceedings of the 3rd International Conference on Renewable Energies Offshore (RENEW 2018), CRC Press, Lisbon, Portugal, 2018, pp. 475–483.
[30] S.J. Ashlin, S.A. Sannasiraj, V. Sundar, Wave forces on an oscillating water column device, Procedia Eng. 116 (2015) 1019–1026.
[31] E. Didier, D.R.C.B. Neves, P.R.F. Teixeira, J. Dias, M.G. Neves, Smoothed particle hydrodynamics numerical model for modeling an oscillating water chamber, Ocean Eng. 123 (2016) 397–410.
[32] D.Z. Ning, R.Q. Wang, Y. Gou, M. Zhao, B. Teng, Numerical and experimental investigation of wave dynamics on a land-fixed OWC device, Energy 115 (2016) 326–337.
[33] R.Q. Wang, D.Z. Ning, C.W. Zhang, Q.P. Zou, Z. Liu, Nonlinear and viscous effects on the hydrodynamic performance of a fixed OWC wave energy converter, Coast. Eng. 131 (2018) 42–50.
[34] C.H. Xu, Z.H. Huang, Three-dimensional CFD simulation of a circular OWC with a nonlinear power-takeoff: model validation and a discussion on resonant sloshing inside the pneumatic chamber, Ocean Eng. 176 (2019) 184–198.
[35] T. Vyzikas, S. Deshoulieres, O. Giroux, M. Barton, D. Greaves, Numerical study of fixed Oscillating Water Column with RANS-type two-phase CFD model, Renew. Energy 102 (2017) 294–305.
[36] P. Boccotti, Design of breakwater for conversion of wave energy into electrical energy, Ocean Eng. 51 (2012) 106–118.
[37] C.-P. Tsai, C.-H. Ko, Y.-C. Chen, Investigation on performance of a modified breakwater-integrated OWC wave energy converter, Sustainability 10 (3) (2018) 643.
[38] I. López, A. Castro, G. Iglesias, Hydrodynamic performance of an oscillating water column wave energy converter by means of particle imaging velocimetry, Energy 83 (2015) 89–103.
[39] S. Jin, R.J. Patton, B. Guo, Viscosity effect on a point absorber wave energy converter hydrodynamics validated by simulation and experiment, Renew. Energy 129 (2018) 500–512.
[40] X.-L. Jiang, Q.-P. Zou, N. Zhang, Wave load on submerged quarter-circular and semicircular breakwaters under irregular waves, Coast. Eng. 121 (2017) 265–277.